

**PHOTOGEOLOGIC MAP OF THE HELLAS BASIN FLOOR, MARS** H. Bernhardt<sup>1</sup>, H. Hiesinger<sup>1</sup>, M. Ivanov<sup>2</sup>, G. Erkeling<sup>1</sup>, O. Ruesch<sup>1</sup>, D. Reiss<sup>1</sup> <sup>1</sup>Institut für Planetologie, Westfälische Wilhelms-Universität, Wilhelm-Klemm-Str. 10, 48149 Münster, Germany (h.bernhardt@uni-muenster.de), <sup>2</sup>Vernadsky Institute, Russian Academy of Sciences, Kosygin St. 19, 119991 Moscow, Russia.

**Motivation:** Hellas Planitia on Mars is the second-largest topographically well-defined impact structure in the Solar System [e.g., 1] and has repeatedly been interpreted as a major sink for volcanic [e.g., 2], glacio-fluvial [e.g., 3] and aeolian [4] materials. The basin hosts a suite of enigmatic landforms, which are unique to this area and whose origins remain unclear, e.g., the “honeycomb” [e.g., 5], “banded” [6], and “reticulate” [e.g., 7] terrains. Despite its significance, the last comprehensive mapping of the entire Hellas basin floor was done in 2001 [8], pre-dating a wealth of new remote sensing data acquired since then. All subsequent publications focused on areas along the rim [e.g., 9,10] or exclusively on specific landforms [e.g., 11]. Therefore, and in order to synthesize all new observations, extrapolations, and interpretations by us and previous authors, we mapped the entirety of the Hellas basin floor at 1:1,000,000 (Fig. 1A,B), producing a 1:2,000,000 DIN-A0 photogeologic map. It is part of an in-depth analysis of the geologic history of the Hellas basin (see abstract #1336) and is intended to serve as a basemap for future investigations, providing better constraints on potential formation mechanisms of the enigmatic landforms.

**Data and methodology:** Initial unit identification and delimitation were performed on mid-infrared data from the Thermal Emission Imaging System (THEMIS) aboard Mars Odyssey. The THEMIS-IR Daytime global mosaic (100 m/px) [12] provides a gapless, homogeneous dataset mostly unaffected by atmospheric dust, which otherwise compromises some visible image data for the Hellas basin floor. To assess thermophysical properties of the surface, we also used the global thermal inertia mosaic based on THEMIS-IR [13]. In addition, we used mid- to high-resolution visible image data from two Mars Reconnaissance Orbiter (MRO) instruments, the Context Camera (CTX; ~6 m/px) [14] and the High Resolution Imaging Science Experiment (HiRISE; 25-50 cm/px) [15,16], as well as Mars Orbiter Narrow Angle Camera (MOC-NA; 1.4 - ~3 m/px) data [17] aboard Mars Global Surveyor (MGS). CTX covers most of the Hellas basin floor, but it is less suitable as a mapping basis as the inter-comparability of images is often limited by changing lighting conditions, variable atmospheric

dust content, and seasonal surface frost. Also due to atmospheric dust, only six images from the High Resolution Stereo Camera (HRSC; 12.5-50 m/px) on Mars Express (MEx) [18,19] show the surface in sufficient quality within the mapping area. Stereographic digital terrain models (DTMs; 50 m/px) based on HRSC images [20] cover ~6% of the mapping area along the northern and eastern basin rim and were used to greatly improve topographic information in those regions, especially on km- to sub-km-sized features. For the remainder of the basin floor, the global DTM by the Mars Orbiter Laser Altimeter (MOLA) with a horizontal resolution of 463 m/px served as topographic base-map [21]. For small-scale features we used MOLA Precision Experiment Data Records (PEDR) with an along-track spacing of 330 m and a vertical resolution of ~1 m [22]. Wrinkle ridges (Fig. 1B, black lines) were mapped on a high pass-filtered MOLA DTM, improving their identification, especially when subdued [11].

We used standard contact types (certain, approximate, inferred, covered) as well as symbology defined by the US Geological Survey and employed the general techniques for planetary mapping as outlined by [23] and refined by [24]. The mapping area comprises the landform-defined basin floor (approximated by the -5,600 m contour; fig. 1B) as well as adjacent units. To supplement our mapping with further unit characterization and interpretation, we also analyzed data from the Gamma Ray Spectrometer (GRS, ~7 km/px) [25] and Thermal Emission Spectrometer (TES; ~3 km/px) on MGS [26]. Previous investigations based on hyperspectral data by both, the Compact Reconnaissance Imaging Spectrometer for Mars (CRISM; 16-20 m/px) on MRO [27,28], as well as the Observatoire pour la Minéralogie, l'Eau, les Glaces et l'Activité (OMEGA) on MEx [29-32], complemented our unit interpretations. In addition to relative dating via stratigraphic analyses (Fig.1C), we acquired absolute model ages by measuring crater-size frequency distributions on nine map units using techniques described in [33,34], with the aid of CraterTool in ArcGIS [35] and CraterStats for plotting and fitting the distributions [36].

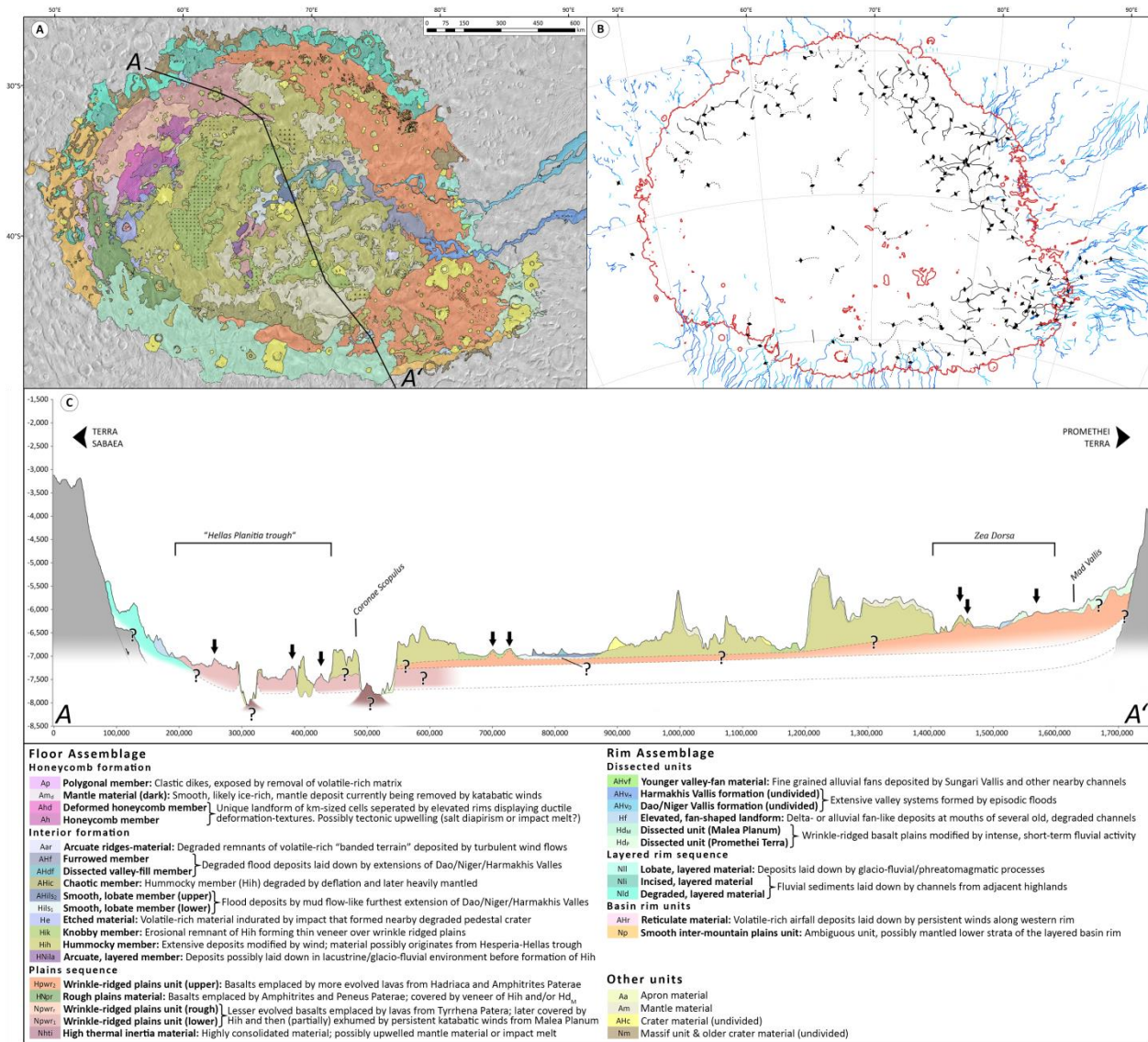


Figure 1: A) Simplified version of our photogeologic map of the Hellas basin floor (orthographic projection centered at 43°S, 69°E; background: THEMIS-IR Daytime 100 m Global Mosaic version 11.6). Black line indicates path of profile shown in (C). B) Same area showing the -5,600 m contour in red, wrinkle ridges in black with diamonds (subdued ridges are dashed), and channel-like valleys in the vicinity of the basin floor in blue (uncertain/highly degraded valleys in light blue). C) MOLA DTM-based profile illustrating our stratigraphic model of the basin floor (path shown in (A)). Black arrows mark wrinkle ridges. Period extents for units labels based on [37]. For more detailed discussions of selected units see abstract #1336.

- References:** [1] Andrews-Hanna, J. C., & Zuber, M. T. (2010) *GSA Special Paper*, 465(01), 1–13. [2] Williams, D. A. et al. (2009) *PSS*, 57(8–9), 895–916. [3] Kargel, J. S., & Strom, R. G. (1992) *Geology*, 20, 3–7. [4] Howard, A. D. et al. (2012) *LPSC* (p. 1105). [5] Moore, J. M., & Wilhelms, D. E. (2001) *Icarus*, 154(2), 258–276. [6] Diot, X. et al. (2014) *PSS*, 1–17. [7] Moore, J. M., & Wilhelms, D. E. (2007) *USGS Geologic Investigations*, 2953, 80225. [8] Leonard, G. L., & Tanaka, K. L. (2001) *USGS Geologic Investigations*, 2694, 80225. [9] Bleamaster, L. F., & Crown, D. A. (2010) *USGS Geologic Investigations*, 3096, 80225. [10] Mangold, N. et al. (2012) *PSS*, 72(1), 18–30. [11] Bernhardt, H. et al. (2014) *LPSC* (p. 1366). [12] Christensen, P. R. et al. (2004) *Space Sci. Rev.*, 110(1/2), 85–130. [13] Christensen, P. R. et al. (2013) *LPSC* (p. 2822). [14] Malin, M. C. et al. (2007) *JGR*, 112(E5), E05S04. [15] McEwen, A. S. (2006) *JGR*, 112. [16] Delamere, W. A. et al. (2010) *Icarus*, 205(1), 38–52. [17] Malin, M. C., & Edgett, K. S. (2010) *The Mars Journal*, 5, 1–60. [18] Neukum, G., & Jaumann, R. (2004) *Mars Express: The Scientific Payload*, 1–19. [19] Jaumann, R. et al. (2007) *PSS*, 55(7–8), 928–952. [20] Gwinner, K. et al. (2009) *Photogrammetric Engineering & Remote Sensing*, 75(9), 1127–1142. [21] Smith, M. D. et al. (2001) *JGR*, 106(E10), 23689. [22] Zuber, M. T., & Smith, M. D. (1992) *JGR*, 97(92), 7781–7797. [23] Wilhelms, D. E. (1990) *Geologic Mapping*. In *Planetary Mapping* (p. 312). [24] Tanaka, K. L. et al. (2009) *PSS*, 57(5–6), 510–532. [25] Boynton, W. V. et al. (2007) *JGR*, 112(E12), E12S99. [26] Putzig, N. (2005) *Icarus*, 173(2), 325–341. [27] Murchie, S. (2007) *JGR*, 112(E5), E05S03. [28] Bandfield, J. L. (2013) *Icarus*, 226(2), 1489–1498. [29] Poulet, F. (2007) *JGR*, 112(E8), E08S02. [30] Williams, D. A. (2010) *EPSL*, 294(3–4), 451–465. [31] Zalewska (Andrzejewska), N. (2013) *PSS*, 78, 25–32. [32] Zalewska (Andrzejewska), N. (2014) Water in the Deepest Crater of Mars. In *Insights on Environmental Changes* (pp. 65–76). [33] Neukum, G. (1983) *Habilitation*, University of Munich. [34] Neukum, G. et al. (2001) *Space Sci. Rev.*, 96, 55–86. [35] Kneissl, T. et al. (2012) *Planet. Space Sci.*, 59, 1243–1254. [36] Michael, G. and Neukum, G. (2010) *Earth Planet. Sci. Lett.*, 294, 223–229. [37] Ivanov, B. A. (2001) *Sp. Sc. Rev.*, 96(1–4), 87–104.